nature photonics

Article

https://doi.org/10.1038/s41566-023-01250-9

A Purcell-enabled monolayer semiconductor free-space optical modulator

In the format provided by the authors and unedited

This PDF file includes:

Supplementary Notes 1-3
Supplementary Figs. 1 to 19

Supplementary Note 1. Modelling the exciton lifetime with an optical rate equation.

We analytically illustrate the relation between the lifetime of the excitons and the gating voltage applied to the optical modulator with an optical rate-equation model [1] as discussed below. We only consider the exciton and trion generation here by assuming that the illumination power is low. An optical rate equation to describe the optical absorption at a steady state induced by the exciton resonance is as follows:

$$G = n_{\mathrm{X}}\left(\gamma_{\mathrm{Xr}} + \gamma_{\mathrm{Xph}} + \gamma_{\mathrm{Xe}} + \gamma_{\mathrm{EX}}\right), \quad (1)$$

$$G_{\mathrm{T}} = n_{\mathrm{X}}\gamma_{\mathrm{EX}} = n_{\mathrm{T}}\gamma_{\mathrm{T}}. \quad (2)$$

G is the generation rate of free electron-hole pairs by illumination, and n_{X} and n_{T} refer to the density of excitons and trions. G_{T} is the generation rate of trions. γ_{EX} denotes the exchange rate of excitons to form trions by combining an additional electron, and γ_{T} is the total decay rate of trions, which is assumed as a constant here to simplify the discussion. γ_{Xr}, γ_{Xph}, and γ_{Xe} correspond to the radiative, phonon-assisted non-radiative, and electron-assisted non-radiative decay rate of excitons. We ignore the hole-assisted scattering here since we focus on an electron-doped system. The phonon-assisted non-radiative decay rate can be estimated from the sum of all the phonon modes that can scatter excitons into a different state [2]. It is expected that when additional electrons are injected into the monolayer semiconductor, the Coulomb interaction between the electron-hole pairs is screened, and therefore the binding energy of excitons is decreased. Consequently, more phonon modes become available to scatter or directly dissociate electron-hole pairs. Given the fact that the electron doping level is low in the solid-state gating configuration (~10^{12}/cm^2), we can apply the Taylor expansion to the phonon-assisted non-radiative decay around the charge neutrality point:

$$\gamma_{\mathrm{Xph}} = \gamma_{\mathrm{Xph0}} + A_{\mathrm{ph1}}n_{\mathrm{e}} + A_{\mathrm{ph2}}{n_{\mathrm{e}}}^2 + \cdots \quad (3)$$

γ_{Xph0} is the phonon-assisted non-radiative decay at the charge neutrality state, and A_{ph1} and A_{ph2} are expansion coefficients. On the other hand, the electron-assisted non-radiative decay rate can be modeled as:

$$\gamma_{\mathrm{Xe}} = A_{\mathrm{e}}n_{\mathrm{e}}. \quad (4)$$

A_{e} represent the capture probabilities for exciton-electron interactions, and n_{e} is the free electron density. The density of excitons and trions can be linked together via a law of mass action:

$$n_{\mathrm{T}} = Tn_{\mathrm{X}}n_{\mathrm{e}}. \quad (5)$$

T denotes the trion formation coefficient. γ_{T} Charge conservation further links the density of trions and electrons to the electron doping level:

$$N = N_{\mathrm{in}} + N_{\mathrm{ex}} = n_{\mathrm{e}} + n_{\mathrm{T}}. \quad (6)$$

N represents the total electron doping density, being the sum of the intrinsic doping N_{in} (defects, charges from substrates) and extrinsic doping $N_{\mathrm{ex}} = c_{ox}V/q$ via electrical gating, where c_{ox} is the oxide capacitance, V is the gating voltage, and q is the electron charge. By combining all these equations together, Eq. (1) can be re-written as:

$$G = n_{\mathrm{X}}\left(\gamma_{\mathrm{X_r}} + \gamma_{\mathrm{Xph0}} + \left(A_{\mathrm{ph1}} + A_{\mathrm{e}} + \gamma_{\mathrm{T}}T\right)\frac{N_{\mathrm{in}} + \frac{c_{\mathrm{ox}}V}{q}}{1 + Tn_{\mathrm{X}}} + A_{\mathrm{ph2}}\left(\frac{N_{\mathrm{in}} + \frac{c_{\mathrm{ox}}V}{q}}{1 + Tn_{\mathrm{X}}}\right)^2\right). \quad (7)$$

When the density of excitons is low ($n_{\mathrm{ex}} \ll n_{\mathrm{e}}$), the above equation can be further simplified as:

$$G \cong n_{\mathrm{X}}(A + BV + CV^2), \quad (8)$$

where

$$A = \gamma_{\mathrm{Xr}} + \gamma_{\mathrm{Xph0}} + \left(A_{\mathrm{ph1}} + A_{\mathrm{e}} + \gamma_{\mathrm{T}}T\right)N_{\mathrm{in}} + A_{\mathrm{ph2}}{N_{\mathrm{in}}}^2, \quad (9)$$

$$B = \left(A_{\mathrm{ph1}} + A_{\mathrm{e}} + \gamma_{\mathrm{T}}T + 2A_{\mathrm{ph2}}N_{\mathrm{in}}\right)\frac{c_{ox}}{q}, \quad (10)$$

$$C = A_{\mathrm{ph2}}\left(\frac{c_{ox}}{q}\right)^2. \quad (11)$$

Equation 8 clearly shows that $A + BV + CV^2$ is the total decay rate of excitons, which can be tuned efficiently via electrical gating as illustrated in Fig. 3c and Supplementary Fig. 12. At the charge neutrality point $N_{\mathrm{in}} + \frac{c_{ox}V}{q} = 0$, the total decay rate of excitons goes back to $\gamma_{\mathrm{Xr}} + \gamma_{\mathrm{Xph0}}$ as expected.

Supplementary Note 2. Detailed temporal coupled mode theory for optical coupling between the exciton resonance and the metasurface in the optical modulator.

To better understand the optical coupling between the exciton resonance and the metasurface in the designed optical modulator, and especially how the reflection modulation can benefit from such an optical coupling, we model the modulator as an optical system consisting of two coupled cavities with one port, and apply a temporal coupled mode theory (CMT) for analysis [3]. The metasurface serves as one of these cavities and facilitates the coupling to free-space photons. It both allows for the resonant optical excitation of quasi-guided surface plasmon polariton (SPP) waves and controls their decoupling back into free space radiation. The resonant excitonic system serves as the second cavity. It can be coherently excited by the SPPs and the excitons can in turn couple back into the metasurface cavity through the coherent re-excitation of SPPs. This coupled dynamics is captured by the following equations:

$$\frac{d}{dt}\begin{pmatrix} a_{\mathrm{cav}} \\ a_{\mathrm{x}} \end{pmatrix} = \begin{pmatrix} \mathrm{i}\omega_{\mathrm{cav}} - \gamma_{\mathrm{cavr}} - \gamma_{\mathrm{cava}} & \mathrm{i}g_{\mathrm{cavx}} - \gamma_0 \\ \mathrm{i}g_{\mathrm{cavx}} - \gamma_0 & \mathrm{i}\omega_{\mathrm{x}} - \gamma_{\mathrm{xr}} - \gamma_{\mathrm{xa}} \end{pmatrix}\begin{pmatrix} a_{\mathrm{cav}} \\ a_{\mathrm{x}} \end{pmatrix} + \begin{pmatrix} \kappa_{\mathrm{cav}} \\ \kappa_{\mathrm{x}} \end{pmatrix} {S_1}^+, \tag{12}$$

where, $a_{\mathrm{cav(x)}}$, $\omega_{\mathrm{cav(x)}}$, $\gamma_{\mathrm{cavr(xr)}}$, $\gamma_{\mathrm{cava(xa)}}$ represent the normalized amplitude, resonant frequency, radiative decay rate, as well as non-radiative decay rate for the optical resonance supported by the metasurface cavity and the exciton resonance, respectively. ${S_1}^+ = e^{i\omega t}$ is the incident plane wave acting as the input of the port, and $\kappa_{\mathrm{cav(x)}}$ is the incoupling constant from the free-space plane wave to the cavity. g_{cavx} represents the direct coupling between the two cavities, and γ_0 quantifies the super- (sub-) radiance when the two cavities emit photons into the same port. The output from the port ${S_1}^-$ is dictated by the scattering matrix:

$${S_1}^- = -{S_1}^+ + d_{\mathrm{cav}} a_{\mathrm{cav}} + d_{\mathrm{x}} a_{\mathrm{x}}, \tag{13}$$

where $d_{\mathrm{cav(x)}}$ represents the outcoupling constant from the cavity to the free-space plane wave. The energy conservation sets up the relation between the outcoupling constant and the radiative decay rates of the cavities:

$$|d_i|^2 = 2\gamma_{\mathrm{ir}}, \qquad {d_{\mathrm{x}}}^* d_{\mathrm{cav}} = 2\gamma_0, \qquad i = \mathrm{x}, \mathrm{cav}. \tag{14}$$

Time reversal symmetry further dictates that the incoupling and outcoupling constant have to satisfy the following relations:

$$\kappa_i = d_i, \qquad {d_i}^* = d_i, \quad i = \mathrm{x}, \mathrm{cav}. \tag{15}$$

After some algebra, we can get:

$$\kappa_i = d_i = \sqrt{2\gamma_{\mathrm{ir}}}, \qquad i = \mathrm{x}, \mathrm{cav}. \tag{16}$$

$$\gamma_0 = \sqrt{\gamma_{\mathrm{cavr}}\gamma_{\mathrm{xr}}}. \tag{17}$$

(1). Steady-state analysis.

By plugging all these relations into the dynamic coupled equations, at the steady state we find:

$$r = \frac{{S_1}^-}{{S_1}^+}$$
$$= -1 + \frac{\frac{\mathrm{i}(g_{\mathrm{cavx}} + \mathrm{i}\sqrt{\gamma_{\mathrm{cavr}}\gamma_{\mathrm{xr}}})2\sqrt{\gamma_{\mathrm{cavr}}\gamma_{\mathrm{xr}}}}{\mathrm{i}(\omega - \omega_{\mathrm{x}}) + \gamma_{\mathrm{xr}} + \gamma_{\mathrm{xa}}} + 2\gamma_{\mathrm{cavr}}}{\mathrm{i}(\omega - \omega_{\mathrm{cav}}) + \gamma_{\mathrm{cavr}} + \gamma_{\mathrm{ava}} + \frac{(g_{\mathrm{cavx}} + \mathrm{i}\sqrt{\gamma_{\mathrm{cavr}}\gamma_{\mathrm{xr}}})^2}{\mathrm{i}(\omega - \omega_{\mathrm{x}}) + \gamma_{\mathrm{xr}} + \gamma_{\mathrm{xa}}}}$$
$$+ \frac{\frac{\mathrm{i}(g_{\mathrm{cavx}} + \mathrm{i}\sqrt{\gamma_{\mathrm{cavr}}\gamma_{\mathrm{xr}}})2\sqrt{\gamma_{\mathrm{cavr}}\gamma_{\mathrm{xr}}}}{\mathrm{i}(\omega - \omega_{\mathrm{cav}}) + \gamma_{\mathrm{cavr}} + \gamma_{\mathrm{cava}}} + 2\gamma_{\mathrm{xr}}}{\mathrm{i}(\omega - \omega_{\mathrm{x}}) + \gamma_{\mathrm{xr}} + \gamma_{\mathrm{xa}} + \frac{(g_{\mathrm{cavx}} + \mathrm{i}\sqrt{\gamma_{\mathrm{cavr}}\gamma_{\mathrm{xr}}})^2}{\mathrm{i}(\omega - \omega_{\mathrm{cav}}) + \gamma_{\mathrm{cavr}} + \gamma_{\mathrm{cava}}}}. \quad (18)$$

The first term in the above equation comes from the reflection from the non-resonant background, while the second and third term corresponds to the light scattering from the metasurface cavity and the excitons, respectively. Given the fact that at room temperature the radiative decay rate of excitons is one order of magnitude smaller than its non-radiative decay rate, the direct coupling strength to the cavity, as well as the decay rate of the metasurface cavity, we may ignore this minor contribution by assuming $\gamma_{\mathrm{xr}} \cong 0$, and therefore we can greatly simplify the above equation as follows:

$$r \cong -1 + \frac{2\gamma_{\mathrm{cavr}}}{\mathrm{i}(\omega - \omega_{\mathrm{cav}}) + \gamma_{\mathrm{cavr}} + \gamma_{\mathrm{cava}} + \frac{(g_{\mathrm{cavx}})^2}{\mathrm{i}(\omega - \omega_{\mathrm{x}}) + \gamma_{\mathrm{x}}(V)}}. \quad (19)$$

We note that $\gamma_{\mathrm{x}}(V)$ represents the total decay rate of excitons in the absence of the optical coupling, which can be tuned via electrical gating V, increasing from $\gamma_{\mathrm{x0}} = \gamma_{\mathrm{xr}} + \gamma_{\mathrm{xa0}}$ at the neutrality point toward infinitely large by additional electron injection. Such a simplified equation gives us a very clear understanding of the role of the tunable exciton resonance in determining the reflection from the designed optical modulator. In the presence of the efficient coupling between the exciton resonance and the metasurface cavity, the exciton excitation effectively becomes an additional tunable non-radiative decay channel of the metasurface cavity $\frac{(g_{\mathrm{cavx}})^2}{\mathrm{i}(\omega - \omega_{\mathrm{x}}) + \gamma_{\mathrm{x}}(V)}$. When the metasurface cavity is on resonance ($\omega = \omega_{\mathrm{cav}}$), the reflection coefficient of the modulator can be further written as:

$$r \cong -1 + \frac{2\eta_{\mathrm{cav}}}{1 + \frac{\Gamma}{\mathrm{i}\delta_{\mathrm{x}} + \gamma_{\mathrm{x}}(V)}}. \quad (20)$$

Here, the term $\eta_{\mathrm{cav}} = \gamma_{\mathrm{cavr}}/(\gamma_{\mathrm{cavr}} + \gamma_{\mathrm{cava}})$ determines the scattering efficiency of the metasurface cavity, and $\Gamma = {g_{\mathrm{cavx}}}^2/(\gamma_{\mathrm{cavr}} + \gamma_{\mathrm{cava}})$ denotes the Purcell-enhanced radiative decay rate of excitons into the metasurface cavity. $\delta_{\mathrm{x}} = \omega_{\mathrm{cav}} - \omega_{\mathrm{x}}$ is the detuning for the coupled

system. When the exciton resonance is turned off ($\gamma_{\mathrm{x}} \sim \infty$), the reflection coefficient of the modulator is simply determined by the scattering efficiency of the metasurface cavity $r_{\max} = 2\eta_{\mathrm{cav}} - 1$, and the near-unity reflection can be achieved if the metasurface cavity is lossless. To maximize the modulation ratio, we need to operate the modulator near the critical coupling point ($r_{\min} = 0$) at the cavity resonant wavelength when the exciton is turned on, leading to the relation $2\eta_{\mathrm{cav}} - 1 = \frac{\Gamma}{\mathrm{i}\delta_{\mathrm{x}} + \gamma_{\mathrm{x0}}}$. It is thus clear that the modulation ($\Delta r = r_{\max} - r_{\min} \sim \frac{\Gamma}{\mathrm{i}\delta_{\mathrm{x}} + \gamma_{\mathrm{x0}}}$) can be efficient only if the Purcell-enhanced radiative decay rate (Γ) becomes comparable to the sum rate of other unwanted decay processes of excitons ($\sim \gamma_{\mathrm{x0}}$), and the exciton resonance degenerates with the metasurface cavity mode ($\delta_{\mathrm{x}} \sim 0$).

We further fit the simulated results with the CMT model to extract the related parameters ($\hbar\gamma_{\mathrm{xr}}$ = 2.3 meV, $\hbar\gamma_{\mathrm{xa0}}$ = 26.6 meV, $\hbar\gamma_{\mathrm{cavr}}$ = 14.4 meV, $\hbar\gamma_{\mathrm{cava}}$ = 4.9 meV, $\hbar g_{\mathrm{cavx}}$ = 17.7 meV) and confirm the validity of the theory as shown in Fig. 2d and Supplementary Fig. 6. During the fitting process, the reflection from the non-resonant background is also treated as a variable r_{b} to take the optical loss from the Ag mirror into account.

We also note that the dephasing of excitons in the WS_2 monolayer should, in principle, also play a role in determining the reflection from the designed optical modulator. The impact of dephasing is not captured by the presented model (beyond possible contributions to the broadening of the exciton linewidth as measured by ellipsometry). A quantum-mechanical model needs to be developed to describe the difference between the self-interference of the exciton emission and its interference with the background reflection in a limited coherence time [4,5]. It is worth noting that both the CMT and full-field simulations describe the same physics and do not fully capture the impact of dephasing processes.

(2). Eigen-mode analysis.

To study the intrinsic properties of the coupled system, we can temporarily turn off the out-coupling channel. Therefore, the dynamic equation can be rewritten as below:

$$\frac{d}{dt}\begin{pmatrix} a_{\mathrm{cav}} \\ a_{\mathrm{x}} \end{pmatrix} = \begin{pmatrix} \mathrm{i}\tilde{\omega}_{\mathrm{cav}} & \mathrm{i}\tilde{g}_{\mathrm{cavx}} \\ \mathrm{i}\tilde{g}_{\mathrm{cavx}} & \mathrm{i}\tilde{\omega}_{\mathrm{x}} \end{pmatrix}\begin{pmatrix} a_{\mathrm{cav}} \\ a_{\mathrm{x}} \end{pmatrix}. \tag{21}$$

In the presence of the efficient coupling between the metasurface cavity and the exciton resonance, two hybridized modes $|\pm\rangle$ occur to replace the unperturbed metasurface cavity mode $|\mathrm{cav}\rangle$ and the exciton mode $|\mathrm{x}\rangle$ as the eigenmodes through the diagonalization of the Hamiltonian of the coupled system. The dynamic equation of the coupled system is then written under the new basis:

$$\frac{d}{dt}\begin{pmatrix} a_{+} \\ a_{-} \end{pmatrix} = \begin{pmatrix} \mathrm{i}\tilde{\omega}_{+} & 0 \\ 0 & \mathrm{i}\tilde{\omega}_{-} \end{pmatrix}\begin{pmatrix} a_{+} \\ a_{-} \end{pmatrix}, \tag{22}$$

where:

$$\mathrm{i}\tilde{\omega}_{\pm} = \mathrm{i}\omega_{\pm} - \gamma_{\pm} = \frac{\mathrm{i}(\tilde{\omega}_{\mathrm{cav}} + \tilde{\omega}_{\mathrm{x}}) \pm \mathrm{i}\sqrt{(\tilde{\omega}_{\mathrm{cav}} + \tilde{\omega}_{\mathrm{x}})^2 - 4\left(\tilde{\omega}_{\mathrm{cav}}\tilde{\omega}_{\mathrm{x}} - \tilde{g}_{\mathrm{cavx}}{}^2\right)}}{2}. \quad (23)$$

$a_{\pm}$ represent the normalized amplitude of the hybridized eigenmodes. The relation between the new basis and the unperturbed basis is given below:

$$|+\rangle = A|\mathrm{cav}\rangle + B|\mathrm{x}\rangle, \quad |-\rangle = C|\mathrm{cav}\rangle + D|\mathrm{x}\rangle, \quad (24)$$

where:

$$A(C) = \frac{\tilde{g}_{\mathrm{cavx}}}{\sqrt{|\tilde{g}_{\mathrm{cavx}}|^2 + \left|\tilde{\omega}_{\pm} - \tilde{\omega}_{\mathrm{cav}}\right|^2}}, \quad B(D) = \frac{\tilde{\omega}_{\pm} - \tilde{\omega}_{\mathrm{cav}}}{\sqrt{|\tilde{g}_{\mathrm{cavx}}|^2 + \left|\tilde{\omega}_{\pm} - \tilde{\omega}_{\mathrm{cav}}\right|^2}}. \quad (25)$$

Therefore, given the initial state of the coupled system to be $|\varphi_0\rangle = a_{\mathrm{cav0}}|\mathrm{cav}\rangle + a_{\mathrm{x0}}|\mathrm{x}\rangle = a_{+0}|+\rangle + a_{-0}|-\rangle$, the time evolution of the coupled system can be expressed as:

$$\begin{aligned} |\varphi(t)\rangle &= a_{+0}e^{\mathrm{i}\tilde{\omega}_{+}t}|+\rangle + a_{-0}e^{\mathrm{i}\tilde{\omega}_{-}t}|-\rangle \\ &= \left(a_{+0}Ae^{\mathrm{i}\tilde{\omega}_{+}t} + a_{-0}Ce^{\mathrm{i}\tilde{\omega}_{-}t}\right)|\mathrm{cav}\rangle \\ &+ \left(a_{+0}Be^{\mathrm{i}\tilde{\omega}_{+}t} + a_{-0}De^{\mathrm{i}\tilde{\omega}_{-}t}\right)|\mathrm{x}\rangle. \end{aligned} \quad (26)$$

We can now switch back to the unperturbed basis to look at the energy hopping between the metasurface cavity mode and the excitons:

$$|a_{\mathrm{cav}}(t)|^2 = \left|a_{+0}Ae^{\mathrm{i}\tilde{\omega}_{+}t} + a_{-0}Ce^{\mathrm{i}\tilde{\omega}_{-}t}\right|^2, \quad |a_{\mathrm{x}}(t)|^2 = \left|a_{+0}Be^{\mathrm{i}\tilde{\omega}_{+}t} + a_{-0}De^{\mathrm{i}\tilde{\omega}_{-}t}\right|^2. \quad (27)$$

Specifically, we can set up the initial state as $|\varphi_0\rangle = |\mathrm{x}\rangle$ to check the decay process of the excitons. By plugging all the extracted parameters from the reflection simulation (Supplementary Fig. 6), the time-resolved exciton decay process for the coupled system is shown in Supplementary Fig. 7. In the presence of the metasurface cavity, the exciton decay rate is accelerated noticeably, indicating that the enhanced radiative decay rate becomes comparable to the rate of other unwanted non-radiative decay and dephasing processes that dominate the population decay in the vacuum. We note that the designed modulator operates in an intermediate regime between the typical weak coupling and strong coupling regime, revealed by the gentle wiggles in the calculated time evolution of the exciton decay process.

(3). Realizing strong coupling in the proposed optical modulator configuration.

Although the designed optical modulator shown in the main text (Figs. 1e, f) operates in the weak coupling regime, we note that the strong coupling can be realized in such a configuration as well. Such a strong coupling occurs uniformly across the entire two-dimensional plane and can be probed directly from the reflection measurement. This is in shape contrast to most of the reported

strong coupling between the excitons and the plasmonic nano-antennas, where only excitons in a very small area in proximity to the nano-antenna can efficiently interact with the nano-antenna, and the mode splitting is only visible in the scattering spectrum via the dark-field measurement.

In order to achieve the strong coupling based on the proposed modulator design, the coupling strength needs to be enhanced by placing the WS_2 monolayer closer to the metasurface gate pad. Additionally, the radiative decay rate of the metasurface cavity can be suppressed by narrowing the width of the groove perturbation on the metasurface gate pad. For example, by reducing the gate oxide thickness from 15 nm to 1 nm (i.e., few-layer hBN) and narrowing the groove width from 78 nm to 5 nm, mode splitting occurs naturally in the simulated reflection spectrum (Supplementary Fig. 8a). The corresponding decay rates can be extracted based on the CMT model ($\hbar\gamma_{\mathrm{cavr}}$ ~ 3.8 meV, $\hbar\gamma_{\mathrm{cava}}$ ~ 4.0 meV, $\hbar g_{\mathrm{cavx}}$ ~ 22.8 meV), and the calculated time evolution of the coupled system visualizes a weak Rabi oscillation resulting from the nature of strong coupling (Supplementary Fig. 8b).

The Rabi oscillation can be further enhanced by reducing the non-radiative decay rate of the excitons, which can be realized by cooling down the sample to cryogenic temperatures. For instance, if we don't change any rates extracted from the design in Supplementary Fig. 8a but set up the non-radiative decay rate of the excitons ($\hbar\gamma_{\mathrm{xa0}}$) as 5 meV, the Rabi oscillation is found to be enhanced significantly from the calculated time evolution of the coupled system (Supplementary Fig. 8c).

Supplementary Note 3. Discussions on further improving the performance of the demonstrated optical modulator.

Although a 10 percentage-point reflection change and a 3 dB modulation ratio are successfully observed in the experiment (Fig. 3 b, c), we admit that there is still a clear gap (~ 4 times) between the performance of the fabricated devices and the ideal ones in the simulations. We attribute this to the weaker exciton resonance in the WS_2 monolayer caused by the additional doping and the inhomogeneous broadening due to the dielectric and charge disorder from ALD Al_2O_3 encapsulation (Supplementary Fig. 13) as compared with a prime sample. In addition, the insubstantial carrier injection limited by a very thin, non-uniform gate insulator restricts the exciton lifetime modulation range. In our experiment, we apply a 3V gating voltage on a 15 nm-thick gate oxide, corresponding to a vertical DC electric field of ~ 0.20 V/nm. This field strength is in the same order as the previously reported result (65 V on a 280 nm-thick SiO_2 gate oxide, corresponding to ~ 0.23 V/nm [6]), but still far away from the breakdown voltage of good-quality ALD Al_2O_3 (~ 1V/nm). However, we do suffer from the relatively low-quality, non-uniform ALD oxide deposited on the WS_2 monolayer, which restricts the applied voltage to 3V in our experiment.

Both challenges mentioned above are linked to the choice of a proper insulating material that can passivate the 2D semiconductors uniformly and hold large enough electric fields to allow more carriers injected into the 2D semiconductors. Hexagonal boron nitride (hBN) is considered as the best candidate so far thanks to its atomically flat nature and wide band gap, and it has been commonly used these days for encapsulation in fundamental 2D semiconductor studies. We envision that, by replacing the ALD Al_2O_3 layer with a multi-layer hBN in the modulator design, the modulation effect in the experiment will be enhanced further and can approach the performance of ideal devices shown in the simulations. Nevertheless, the major limitation of hBN encapsulation is that the hBN layer prepared by mechanical exfoliation can only provide a tens-of-micrometer-sized encapsulation area each time, and precise alignment is required during the transfer process. Therefore, even if we may be able to fabricate a few devices from this method (which should be good enough for fundamental studies), we cannot extend this concept to chip- or wafer-scale manufacture.

We want to emphasize that, in the design of practical optoelectronic devices, the scalability for mass production is as much important as the optimal performance of a single device that we can achieve. Given the fact that many high-performance devices based on 2D semiconductors have been reported, scalability has become the major challenge to prevent us from commercializing 2D semiconductor-based devices. From this point of view, we sincerely believe that the successful demonstration of a 2D semiconductor-based optical modulator array using all standard cleanroom processing is very meaningful to the community. For this reason, although it has been proved in our experiment that the ALD Al_2O_3 may not be the best choice for maximizing the device performance, it seems to be the only mature standard cleanroom processing that allows us to pattern modulators in the chip scale at this moment.

We are optimistic about improving the device performance while maintaining scalability in mass production in the future. Chemical vapor deposition and molecular beam epitaxy have been proved to be able to grow reasonably high-quality 2D semiconductors [7,8] and hBN layers [9,10] in the wafer scale, and the comprehensive 2D layer transfer system is also developed recently [11,12]. There is no doubt that all these emerging technologies will greatly facilitate the mass production of electronic and optoelectronic devices based on 2D semiconductors in a systematic way.

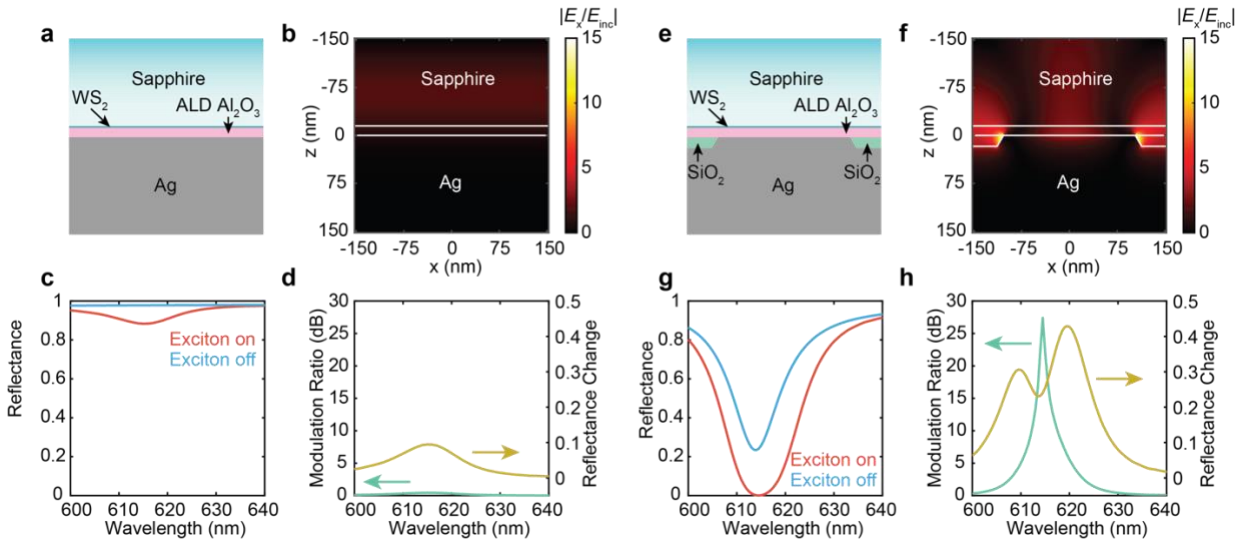

Supplementary Fig. 1 | Optical modulation with a conventional flat Ag gate pad. a, Detailed cross-sectional geometry and **b,** the corresponding electric-field distribution of the conventional optical modulator with a flat Ag gate pad under the normally incident plane-wave illumination. The incident wavelength is 615 nm. **c,** Simulated reflection spectra of the conventional optical modulator under plane-wave illumination. The exciton resonance in WS_2 is switched on (orange) and off (blue) artificially by first separating the exciton resonance contribution from the dielectric background in the dielectric function of the WS_2 monolayer and then keeping (on-state) or removing (off-state) this contribution in the dielectric function. **d,** Extracted modulation ratio (green) and absolute reflectance change (yellow) from the simulations in **c**. **e-h,** Copied from Figs. 1c-f in the main text for a direct comparison.

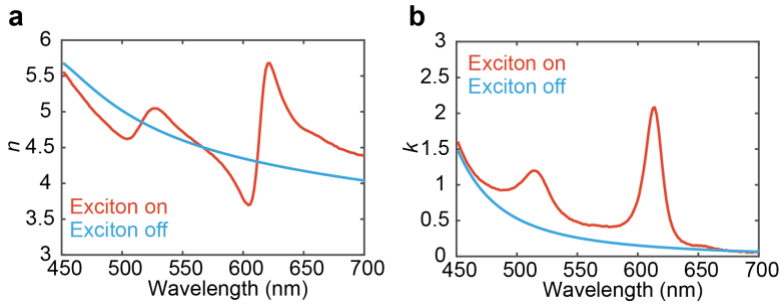

Supplementary Fig. 2 | Refractive-index change of a WS_2 monolayer when the exciton resonance is switched on and off artificially. a, Real and **b,** imaginary part of the refractive index of a WS_2 monolayer when the exciton resonance is switched on (neutral state) and off (electron-doped state). The refractive index used for the 'exciton on' status is determined by ellipsometry measurements on a commercially available (2D Semiconductors) chemical-vapor-deposition (CVD) grown WS_2 monolayer on a sapphire substrate. We assume that this sample is close to the charge neutrality point, and therefore the exciton resonance is not damped. The dielectric background of the WS_2 monolayer, which is used to calculate the dielectric constant for the 'exciton off' status, is then separated from the exciton resonance contribution by fitting the dielectric constant from the ellipsometry measurement with two Lorentz oscillators for the A and B excitons and a Tauc-Lorentz oscillator for the inter-band transitions as the background.

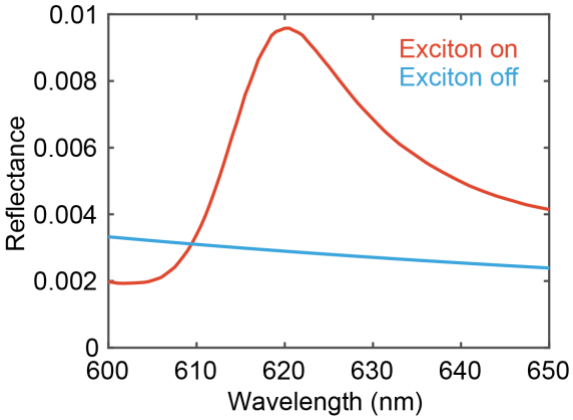

Supplementary Fig. 3 | Reflection modulation with a suspended WS_2 monolayer. The figure shows the simulated reflection spectra of a suspended WS_2 monolayer when the exciton resonance is switched on and off artificially. Only a ~0.6 percentage-point reflection change is observed, originating from the limited light scattering from the exciton resonance due to the much smaller intrinsic radiative decay rate of excitons compared with its non-radiative decay and dephasing rate.

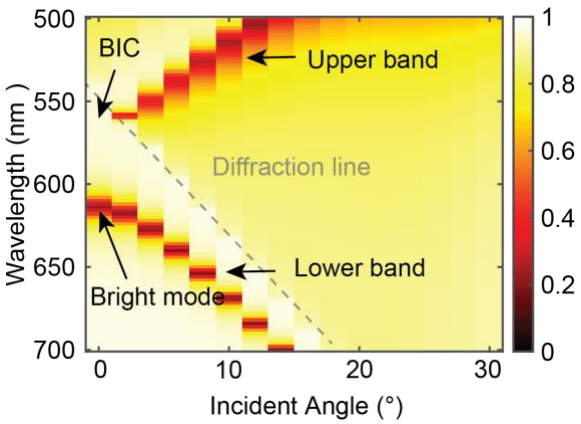

Supplementary Fig. 4 | Optical modes supported by the Ag metasurface gate pad. The figure shows the simulated reflection spectra of the designed optical modulator as a function of the incident angle under TM-polarized illumination. We find two photonic bands in the wavelength range we study here. These photonic bands originate from the dispersion relation of the surface plasma polaritons at the Ag/dielectric interface. At Γ point, the mode from the lower band can be excited efficiently by the free-space light, leading to a clear dip in the reflection spectrum. Meanwhile, the mode from the upper band disappears at Γ point. This results from the fact that this mode has an anti-symmetric electric-field distribution in each period, and therefore cannot be excited by the normally incident plane wave for the symmetry reason. Such a mode is also commonly referred to as symmetry-protected bound states in the continuum (BIC).

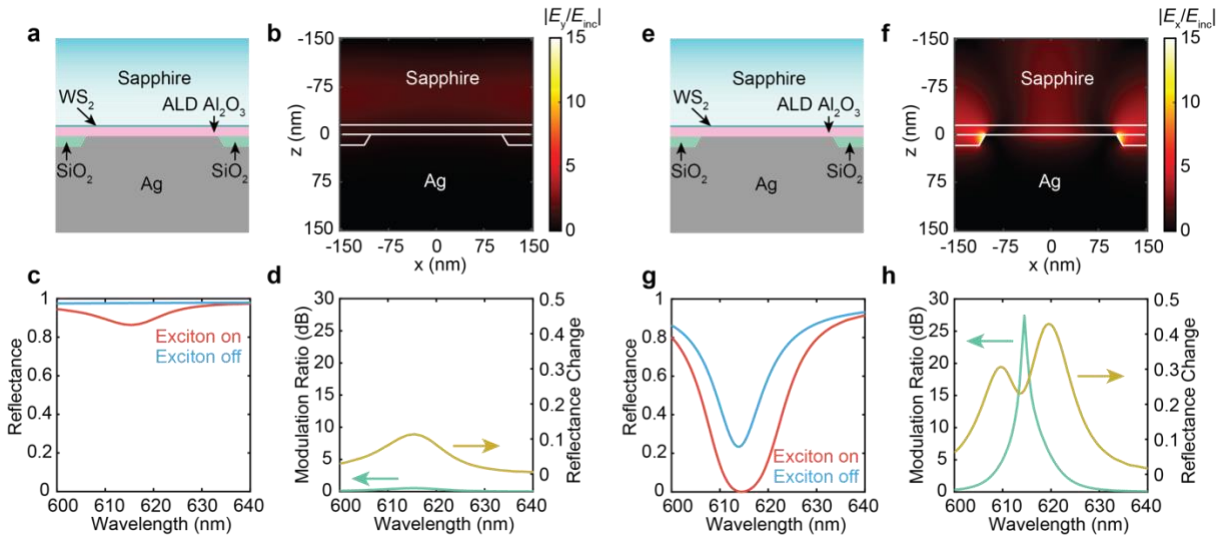

Supplementary Fig. 5 | Optical modulation with a metasurface Ag gate pad under TE-polarized illumination. a, Detailed cross-sectional geometry and **b,** the corresponding in-plane electric-field distribution of the designed optical modulator under TE-polarized plane-wave illumination. The incident wavelength is 615 nm. **c,** Simulated reflection spectra of the designed optical modulator under TE-polarized plane-wave illumination. The exciton resonance in WS_2 is turned on (orange) and off (blue) artificially by first separating the exciton resonance contribution from the dielectric background in the dielectric function of the WS_2 monolayer and then keeping (on-state) or removing (off-state) this contribution in the dielectric function. **d,** Extracted modulation ratio (green) and absolute reflectance change (yellow) from the simulations in **c**. **e-h,** Copied from Figs. 1c-f in the main text for a direct comparison with the TM-polarized illumination.

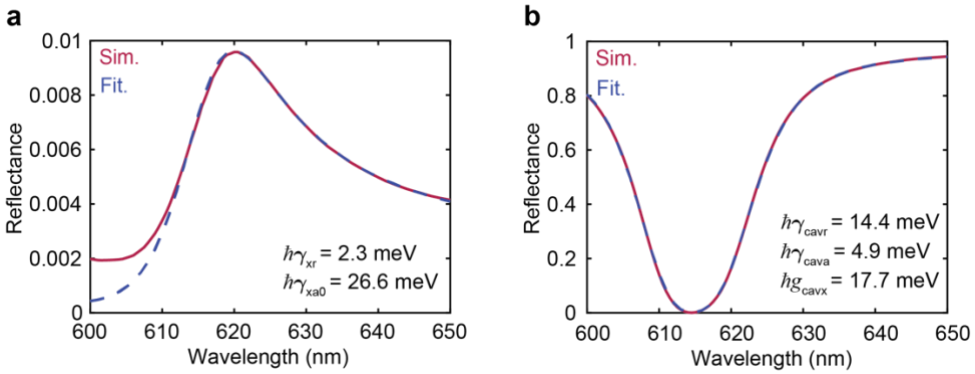

Supplementary Fig. 6 | Extracting the decay rates of excitons into different channels by fitting the temporal coupled mode theory model with the full-field simulation results. a, Simulated and fitted reflection spectrum of a suspended WS_2 monolayer and **b,** the designed optical modulator. From the curve fitting, we find that the non-radiative decay rate of excitons ($\hbar\gamma_{\mathrm{xa0}}$ ~ 26.6 meV) is one order of magnitude larger than its radiative decay rate ($\hbar\gamma_{\mathrm{xr}}$ ~ 2.3 meV). In sharp contrast, the Purcell-enhanced radiative decay rate of excitons in the designed optical modulator ($\Gamma = {g_{\mathrm{cavx}}}^2/(\gamma_{\mathrm{cavr}} + \gamma_{\mathrm{cava}})$) is enhanced significantly (16.2 meV), ~ 7 times larger than its intrinsic radiative decay rate. The comparable Purcell-enhanced radiative decay rate of excitons to its non-radiative decay rate lays the foundation of efficient optical modulation. The non-perfect fitting in **a** results from the fact that the dispersion of the dielectric background of the WS_2 monolayer is not considered in the CMT model.

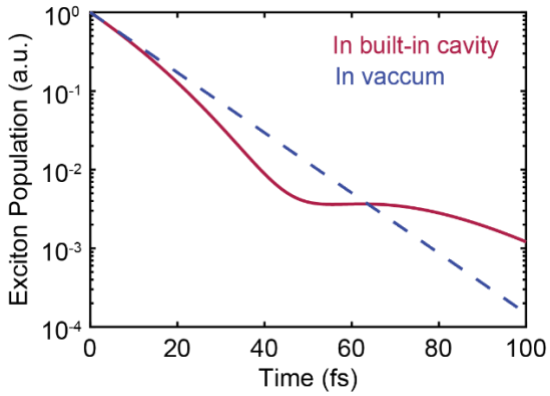

Supplementary Fig. 7 | Accelerated exciton decay process in the coupled system. The red curve shows the time evolution of the exciton decay process when the WS_2 monolayer is embedded in the metasurface cavity (i.e., the proposed modulator configuration), while the blue curve shows the case when the WS_2 monolayer is suspended in the vacuum. In the first 50 fs, the exciton decays notably faster when coupled with the metasurface cavity, indicating that the Purcell-enhanced radiative decay rate becomes comparable to the rate of other unwanted decay channels which dominate the decay process in the vacuum. Gentle wiggles in the red curve reveal that the coupled system falls into an intermediate regime between the typical weak coupling and strong coupling regime.

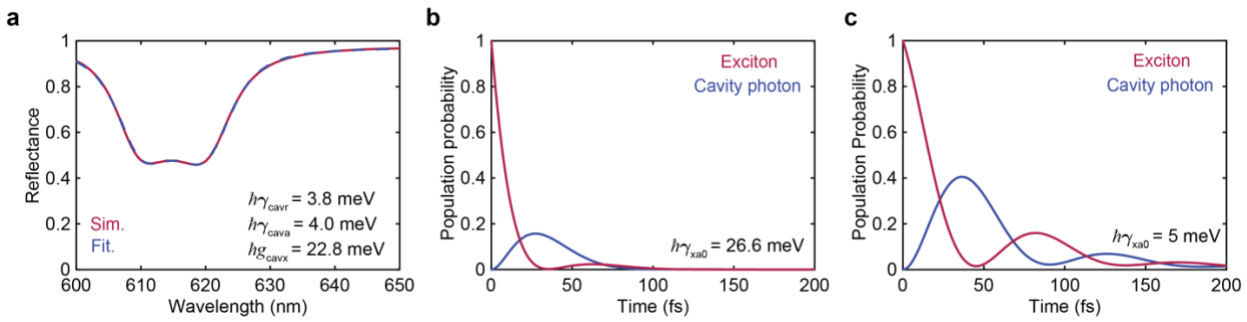

Supplementary Fig. 8 | Realizing strong coupling using a slightly different modulator design. **a,** Simulated (red) and fitted (blue) reflection spectra of the optical modulator with a 1 nm-thick gate oxide. The double-dip lineshape indicates that a strong coupling occurs. **b,** Time evolution of the coupled system that is simulated in **a**. A weak Rabi oscillation is observed. **c,** Time evolution of an optimized coupled system, where the non-radiative decay rate of the excitons is reduced to 5 meV.

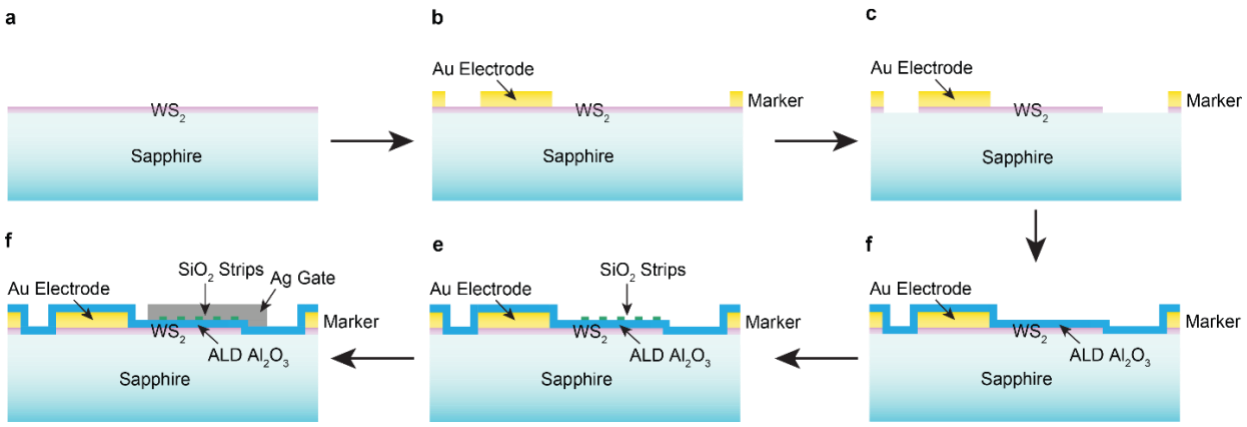

Supplementary Fig. 9 | Schematic of the fabrication process of the monolayer WS_2 free-space optical modulator. a, A piece of mm-scale WS_2 monolayer is prepared on a sapphire substrate. **b,** Au electrode and marker patterning. **c,** WS_2 monolayer pad isolation. **d,** Gate oxide deposition. **e,** SiO_2 nano-strip patterning. **f,** Ag top gate pad patterning.

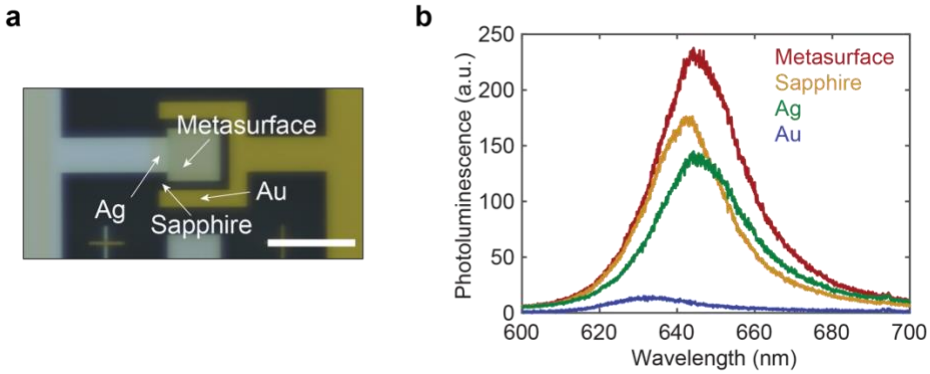

Supplementary Fig. 10 | Spectrally resolved photoluminescence measurements on the fabricated optical modulator. a, Optical image of the fabricated optical modulator. The arrows indicate the positions where we collect the photoluminescence spectra. Scale bar: 50 μm. **b,** Measured photoluminescence spectra at different positions of the fabricated optical modulator. A polarizer is inserted to only collect the TM-polarized photon emission. We find that the photoluminescence is enhanced for the WS_2 monolayer placed on top of the metasurface gate pad due to the Purcell enhancement, while the photon emission is almost killed for the WS_2 monolayer attached to the Au electrode thanks to the quenching effect. We note that a 532 nm green laser is used to pump the WS_2 monolayer in the experiment. This wavelength doesn't overlap with any optical resonance supported by the fabricated optical modulator for absorption enhancement.

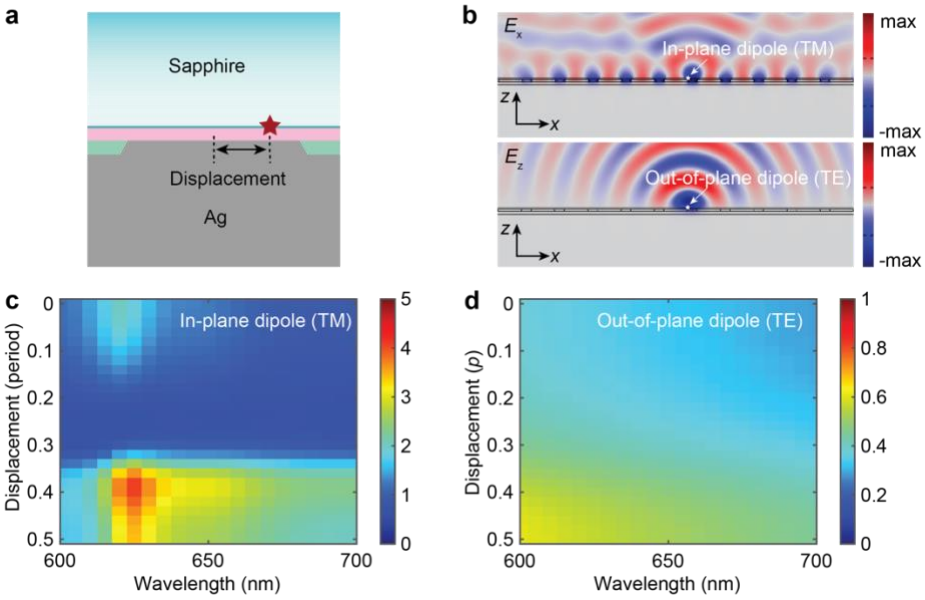

Supplementary Fig. 11 | Simulated Purcell enhancement of the exciton emission in the designed optical modulator. a, Illustration of the geometry used in the simulations. A linear electric dipole (red star) is placed in the plane of the WS_2 monolayer, displaced from the center of one specific period of the metasurface gate pad. **b,** Simulated electric-field distributions of the emission from a linear dipole (white star) placed on top of the metasurface gate pad. **c,** Simulated Purcell enhancement of an in-plane (TM) linear dipole as well as **d,** an out-of-plane (TE) linear dipole placed on top of the metasurface gate pad as a function of the dipole position and its emission wavelength. We note here that this simulation is conducted for linear dipoles in a 2D domain, and therefore may have a qualitative difference from point-dipole 3D simulations. Nevertheless, it captures the nature of the spatially dependent and polarized emission qualitatively.

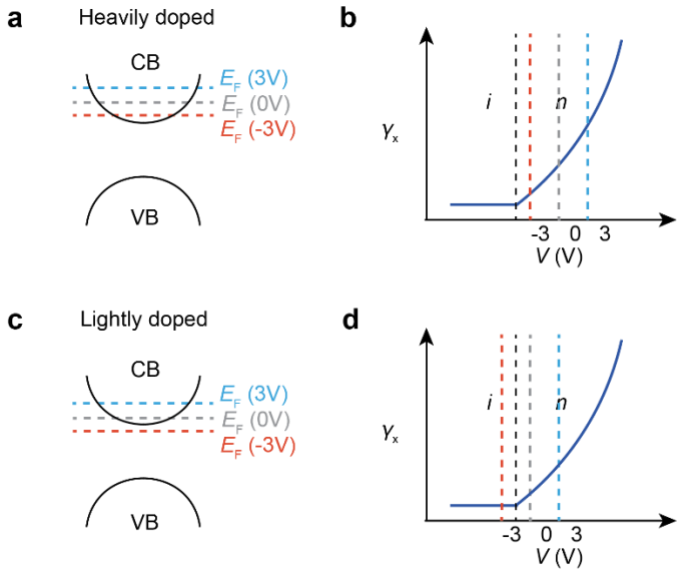

Supplementary Fig. 12 | Illustration of the Fermi-level tuning in the fabricated modulators via electrical gating. In the experiment, we find that the most efficient optical modulation is achieved from different electrical gating ranges for different samples. For example, the fabricated optical modulator exhibits an efficient modulation from -3V to 0V (Fig. 3b), while the fabricated light-field modulator is modulated most efficiently from 0V to 3V (Fig. 4f). We attribute this to the fact that the doping level of WS_2 monolayer in the as-fabricated device is different, and the reflection modulation is not linearly proportional to the change of the doping level. **a, b,** For a heavily doped WS_2 monolayer (e.g, in the fabricated optical modulator), the exciton resonance is already almost switched off (corresponding to a large exciton decay rate) before electrical gating. Therefore, additional hole injection contributes more to the optical modulation as it brings the material back to its neutral state and switches on the exciton resonance gradually. **c, d,** For a lightly doped WS_2 monolayer (e.g, in the fabricated light-field modulator), additional electron injection contributes more to the optical modulation to switch off the exciton resonance gradually. The plotted schematic of the relevant part of the WS_2 band structure and the dependence of the exciton decay rate with the gating voltage explain the above analysis graphically.

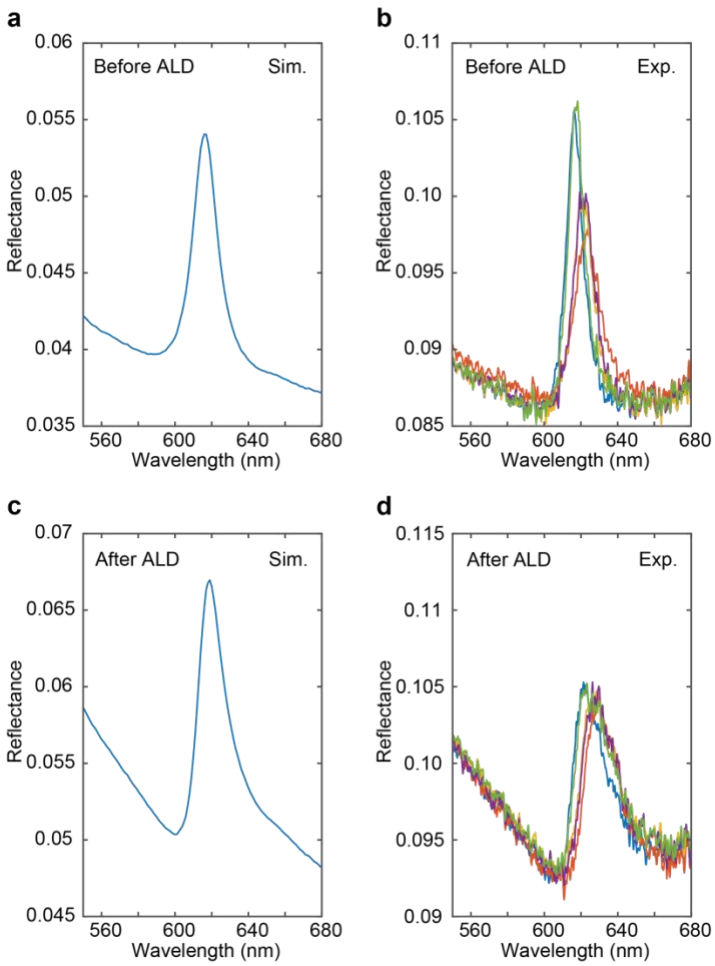

Supplementary Fig. 13 | Weaker exciton resonance observed in the fabricated modulator compared with the prime sample. a, Simulated and **b,** measured reflection spectra from five isolated WS_2 pads on a fused silica substrate before ALD Al_2O_3 encapsulation. **c,** Simulated and **d,** measured reflection spectra from the same five isolated WS_2 pads on the fused silica substrate after ALD AL_2O_3 encapsulation. We note that, the refractive index of the WS_2 monolayer used in the simulations is determined by ellipsometry measurements on a commercially available (2D Semiconductors) chemical-vapor-deposition (CVD) grown WS_2 monolayer on a sapphire substrate. As a result, it should be considered as a realistic bench marker by already taking the inhomogeneous broadening into account. Therefore, we find that the simulated reflection spectrum is consistent with the measured reflection spectra before ALD encapsulation. However, the ALD encapsulation is found to have a major negative impact on the intensity of the exciton resonance, caused by the additional doping and the dielectric and charge disorder from the ALD layer. What' more, a ~ 5 nm spectral shift of the exciton resonance is observed as well, which is attributed to the dielectric screening from the ALD layer. The overall higher reflectance observed in the measurements comes from the additional reflection from the back side of the substrate.

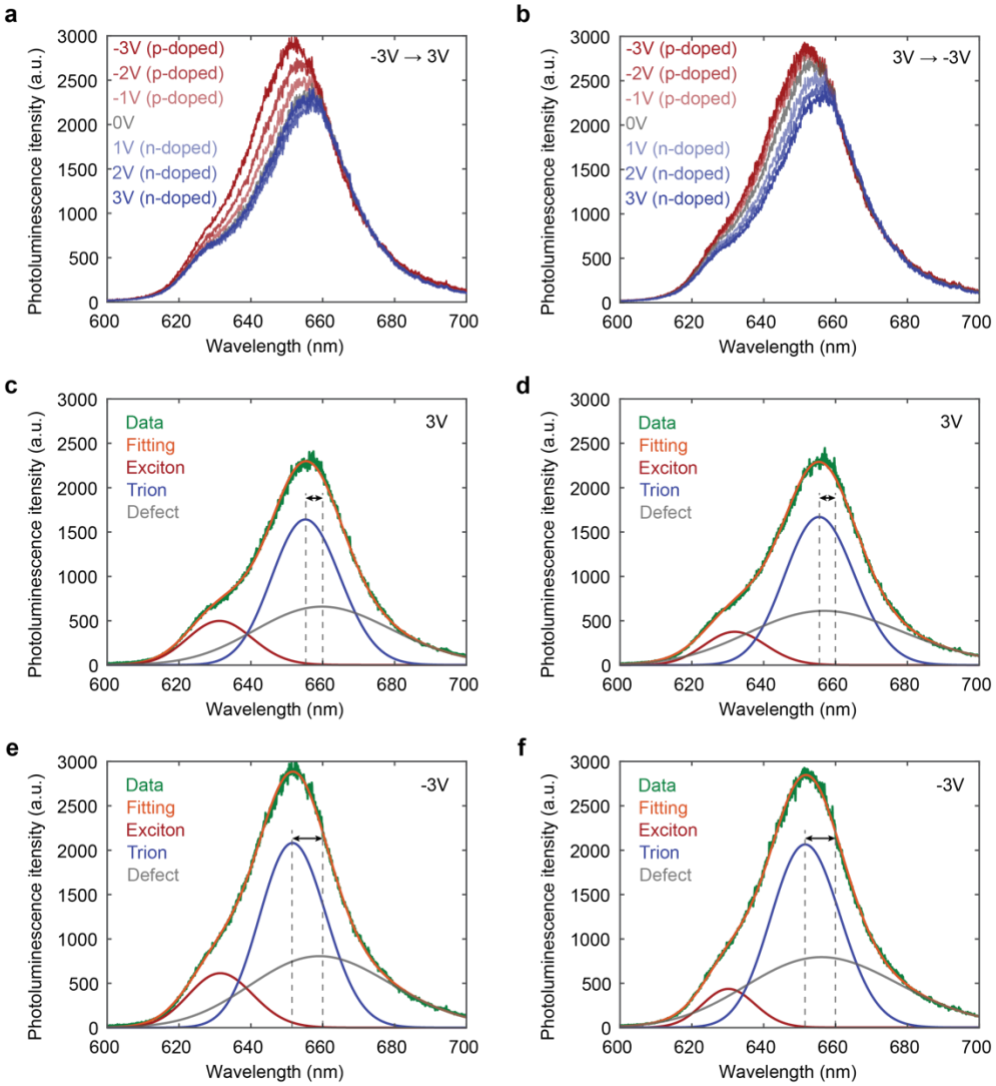

Supplementary Fig. 14 | Photoluminescence spectrum modulation of the WS_2 monolayer in the fabricated optical modulator. a, Measured photoluminescence spectra of the fabricated optical modulator when the gating voltage changes gradually from -3 V (hole injection) to 3 V (electron injection). **b,** The same measurement as **a** but the gating voltage changes from 3 V to -3 V. **c,** Gaussian fits to the measured photoluminescence in **a** at 3 V and **e,** -3 V. **d,** Gaussian fits to the measured photoluminescence in **b** at 3 V and **f,** -3 V. Three Gaussian line shapes are used to fit the measured photoluminescence spectra, corresponding to the exciton, trion, and defect-mediated recombination. We find that the photoluminescence is enhanced via hole injection by suppressing the electron-assisted non-radiative recombination. In addition, redshifts in the photoluminescence from trion recombination are observed with the increased doping level, being consistent with the previous study [13,14]. A hysteresis is also observed in the measurement, possibly due to the bias stress effect from the trapped states in the gate oxide or at the interface [15].

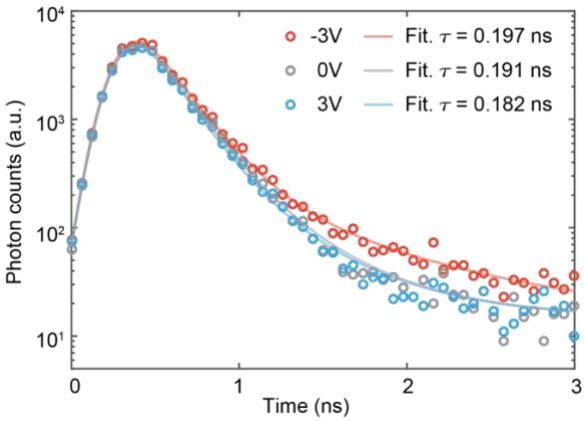

Supplementary Fig. 15 | Photoluminescence lifetime modulation of the WS_2 monolayer in the fabricated optical modulator. The figure shows the time-resolved photoluminescence decay traces with different gating voltages (shown in different colored dots). We note that due to the limited time resolution of the photodiode and the comparable instrument response function (IRF) to the decay rate of excitons, it is hard to extract the accurate lifetime of the exciton/trion emission from the WS_2 monolayer. Nevertheless, the lifetime modulation is recognizable in the measured data. We fit the measured time traces with a bi-exponential decay convolved with the IRF as shown in the different colored semi-transparent curves. We find that the lifetime of the dominant component (exciton/trion emission) decreases with electron injection, being consistent with the developed rate-equation model, while the second, much weaker component can be attributed to the defect-mediated recombination.

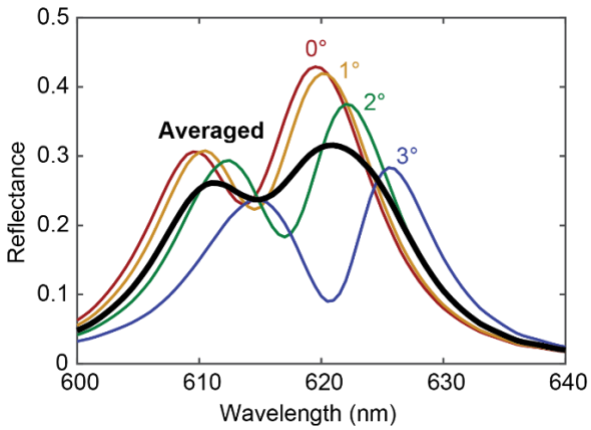

Supplementary Fig. 16 | Spectrally averaged reflection modulation with focused-beam illumination. The figure shows the simulated spectra of the absolute reflection change for the designed optical modulator under plane-wave illumination with the incident angles from 0° to 3° (different colored curves). We find that these spectra shift gradually as we increase the incident angle, originating from the dispersion of the optical mode supported by the Ag metasurface gate pad. The black curve is the spectrum of the averaged absolute reflection change under plane-wave illumination with incident angles from 0° to 3°. A relatively flat modulation plateau is found in the black curve (from 610 nm to 625 nm). This is consistent with the measured results (Fig. 3d), revealing the possibility to modulate optical beams with a certain bandwidth (~ 15 nm) as well.

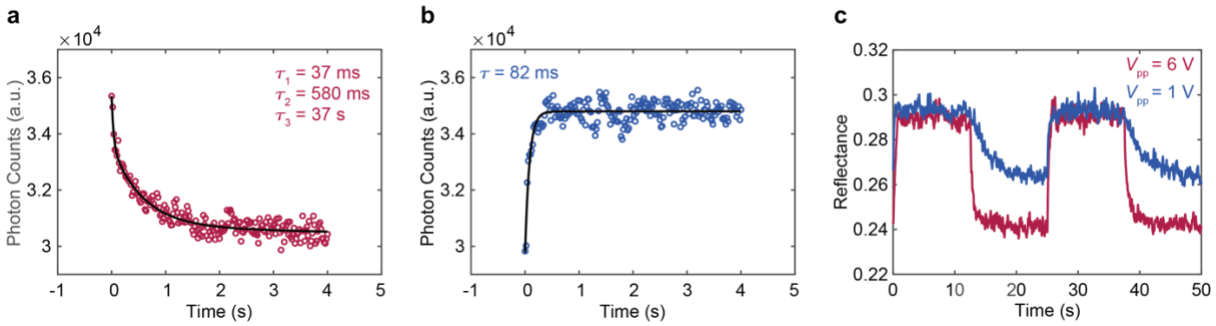

Supplementary Fig. 17 | Measured RC time constant of the fabricated optical modulator. a, Time traces of fall and **b,** rise of the reflected beam with an AC modulation. **c,** Measured reflected beam with an AC modulation with different peak-to-peak voltages. The rise time is measured to be 82 ms, while the fall time is phenomenologically fitted to a tri-exponential decay with time constants of 37 ms, 580 ms, and 37 s. We attribute this large, asymmetric, and varying RC time constant to the giant contact resistance caused by the Schottky junction at the WS_2/gold interface, as well as the large access resistance of the ungated WS_2 monolayer. The signature of the Schottky junction is further revealed by the super slow charging time when a small peak-to-peak voltage (1 V) is applied.

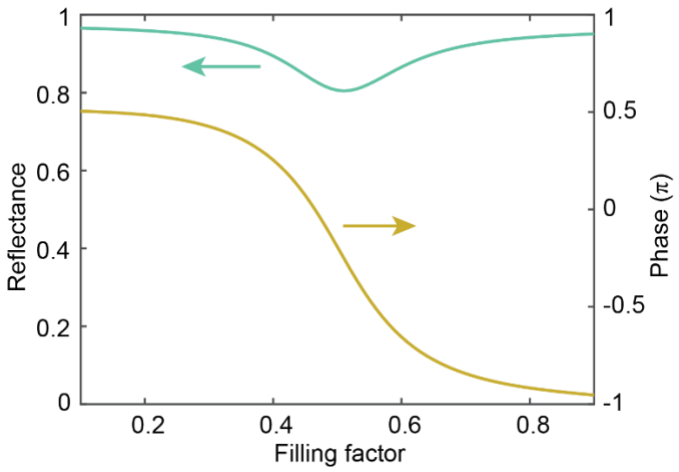

Supplementary Fig. 18 | A 2π full-phase control with an Ag metasurface gate pad. The figure shows the simulated reflectance and reflected phase of the designed light-field modulator as a function of the filling factor of the Ag bump. The exciton resonance is switched off artificially and the incident wavelength is set as 615 nm. The modulator operates in the over-coupling regime to achieve the 2π full-phase control. However, we note that the above simulations are performed under periodic conditions. Thanks to the propagation nature of surface plasmon polaritons at the metal-dielectric interface, a significant optical coupling is expected between the neighboring grooves in the metasurface gate pad. Such a coupling seriously impedes the validity of estimating local reflected phases from simulations under periodic conditions. To overcome this issue, we need to treat the entire supercell in a blazed grating as a whole to estimate its diffraction efficiency and perform a global optimization to improve it.

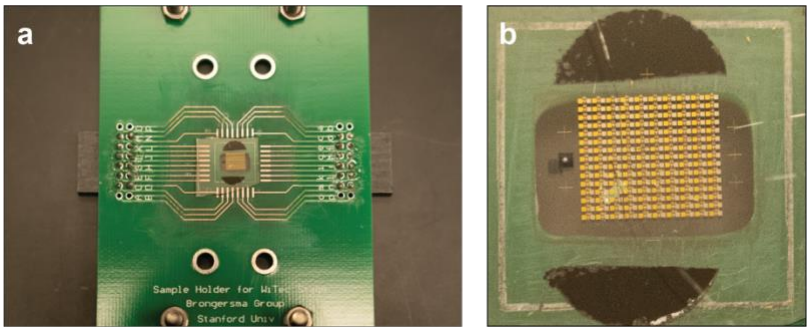

Supplementary Fig. 19 | Preparation for electrical gating experiment. a, Photograph of a homemade printed circuit board with a chip attached to it. **b,** Zoom-in image of the attached chip, where a device array consisting of 150 optical modulators is patterned. Electrodes and top gate pads are wire bonded to the printed circuit board.

References:

1. Lien, D.-H. *et al.* Electrical suppression of all nonradiative recombination pathways in monolayer semiconductors. *Science* **364**, 468–471 (2019).
2. Selig, M. *et al.* Excitonic linewidth and coherence lifetime in monolayer transition metal dichalcogenides. *Nat. Commun.* **7**, 13279 (2016).
3. Fan, S., Suh, W. & Joannopoulos, J. D. Temporal coupled-mode theory for the Fano resonance in optical resonators. *J. Opt. Soc. Am. A* **20**, 569 (2003).
4. Scuri, G. *et al.* Large Excitonic Reflectivity of Monolayer MoSe2 Encapsulated in Hexagonal Boron Nitride. *Phys. Rev. Lett.* **120**, 037402 (2018).
5. Epstein, I. *et al.* Near-Unity Light Absorption in a Monolayer WS 2 Van der Waals Heterostructure Cavity. *Nano Lett.* **20**, 3545–3552 (2020).
6. Yu, Y. *et al.* Giant Gating Tunability of Optical Refractive Index in Transition Metal Dichalcogenide Monolayers. *Nano Lett.* **17**, 3613–3618 (2017).
7. Kang, K. *et al.* High-mobility three-atom-thick semiconducting films with wafer-scale homogeneity. *Nature* **520**, 656–660 (2015).
8. Wang, J. *et al.* Dual-coupling-guided epitaxial growth of wafer-scale single-crystal WS2 monolayer on vicinal a-plane sapphire. *Nat. Nanotechnol.* **17**, 33–38 (2022).
9. Chen, T.-A. *et al.* Wafer-scale single-crystal hexagonal boron nitride monolayers on Cu (111). *Nature* **579**, 219–223 (2020).
10. Kim, S. M. *et al.* Synthesis of large-area multilayer hexagonal boron nitride for high material performance. *Nat. Commun.* **6**, 8662 (2015).
11. Kang, K. *et al.* Layer-by-layer assembly of two-dimensional materials into wafer-scale heterostructures. *Nature* **550**, 229–233 (2017).
12. Mannix, A. J. *et al.* Robotic four-dimensional pixel assembly of van der Waals solids. *Nat. Nanotechnol.* **17**, 361–366 (2022).
13. Morozov, S., Wolff, C. & Mortensen, N. A. Room-Temperature Low-Voltage Control of Excitonic Emission in Transition Metal Dichalcogenide Monolayers. *Adv. Opt. Mater.* **9**, 2101305 (2021).
14. Mak, K. F. *et al.* Tightly bound trions in monolayer MoS2. *Nat. Mater.* **12**, 207–211 (2013).
15. Datye, I. M. *et al.* Reduction of hysteresis in MoS 2 transistors using pulsed voltage measurements. *2D Mater.* **6**, 011004 (2018).